nature portfolio

https://doi.org/10.1038/s41565-021-00881-9

Supplementary information

Electrically reconfigurable non-volatile metasurface using low-loss optical phase-change material

In the format provided by the authors and unedited

nature portfolio

https://doi.org/10.1038/s41565-021-00881-9

Supplementary information

Electrically reconfigurable non-volatile metasurface using low-loss optical phase-change material

In the format provided by the authors and unedited

Supplementary Information

Electrically Reconfigurable Nonvolatile Metasurface Using Low-Loss Optical Phase Change Material

Yifei Zhang[1], Clayton Fowler[2], Junhao Liang[1], Bilal Azhar[1], Mikhail Y. Shalaginov[1], Skylar Deckoff-Jones[1], Sensong An[2], Jeffrey B. Chou[3], Christopher M. Roberts[3], Vladimir Liberman[3], Myungkoo Kang[4], Carlos R ós[1], Kathleen Richardson[4], Clara Rivero-Baleine[6], Tian Gu[1,5], Hualiang Zhang[2,*], and Juejun Hu[1,*]

[1]Department of Materials Science & Engineering, Massachusetts Institute of Technology, Cambridge, MA, USA
[2]Department of Electrical & Computer Engineering, University of Massachusetts Lowell, Lowell, MA, USA
[3]Lincoln Laboratory, Massachusetts Institute of Technology, Lexington, MA, USA
[4]The College of Optics & Photonics, Department of Materials Science and Engineering, University of Central Florida, Orlando, FL, USA
[5]Materials Research Laboratory, Massachusetts Institute of Technology, Cambridge, MA, USA
[6]Missiles and Fire Control, Lockheed Martin Corporation, Orlando, FL, USA

*hualiang_zhang@uml.edu, hujuejun@mit.edu

This Supplementary Information comprises the following Sections:

I. Geometric optimization of heater design

II. Active metasurface design and measurement

III. Evaluation of GSST meta-atom crystallization kinetics

IV. Huygens' surface beam deflector design

V. Future outlook

DISTRIBUTION STATEMENT A. Approved for public release. Distribution is unlimited.
This material is based upon work supported by the Assistant Secretary of Defense for Research and Engineering under Air Force Contract No. FA8702-15-D-0001. Any opinions, findings, conclusions or recommendations expressed in this material are those of the author(s) and do not necessarily reflect the views of the Assistant Secretary of Defense for Research and Engineering.

Section I – Geometric optimization of heater design

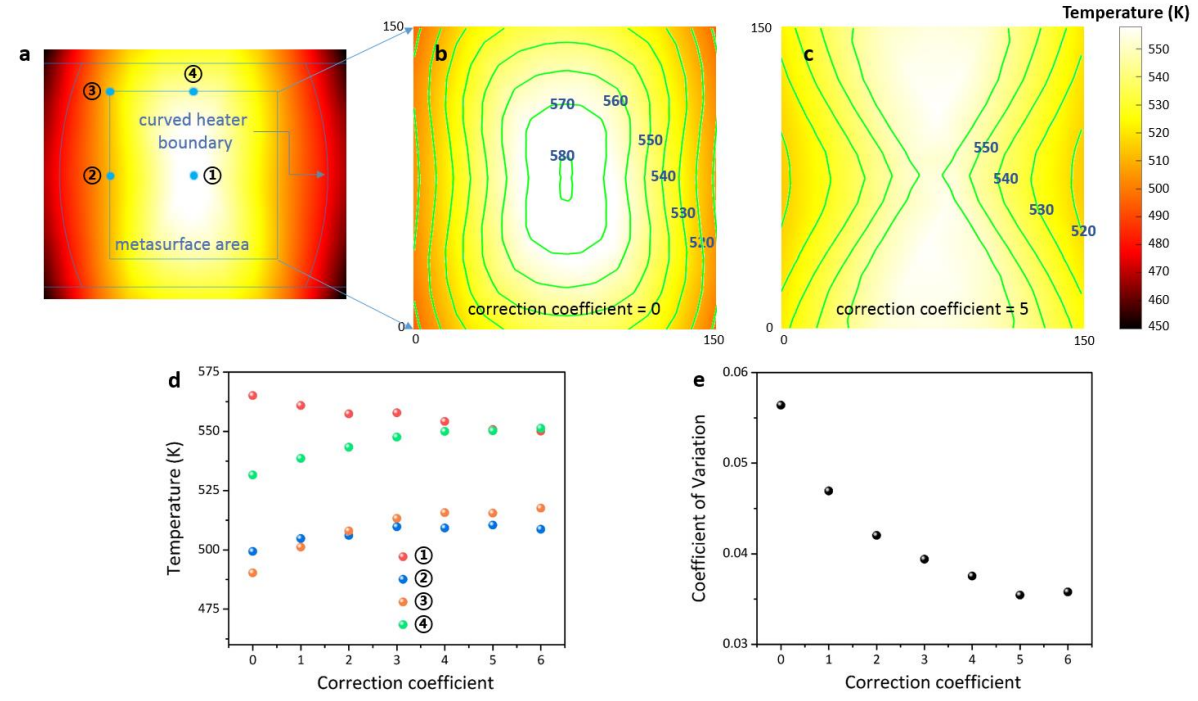

Fig. S1. (a) Schematic showing the curved heater boundary and the metasurface area on the heater. (b, c) Simulated steady-state temperature profiles within the metasurface aperture on the surfaces of (b) a classical square-shaped heater; and (c) an optimized heater with curved boundaries. (d) Temperature at four representative points on the heater surface (labeled in Fig. S1a) as a function of the correction coefficient. (e) Coefficient of temperature variation at the four representative points as a function of the correction coefficient.

The design rationale of the geometric optimization of micro-heaters is to increase the heater width at the center in order to decrease the current density and hence lowering heat generation in the center area. We use a parabolic curve to replace the straight boundaries in the original square heater. The axis of symmetry of the parabola passes through the center of the heater. The correction coefficient defines the curvature of the parabola by the following parametric equation: $x = \pm w/2 \mp a \times 10(2y/w^2 - 1)$, where w is the original width of the heater (200 μm) and a is the correction coefficient. $a = 0$ corresponds to the straight boundary case.

Figure S1 analyzes the temperature profile within the metasurface area to guide the geometrical optimization. Four representative points in the area are used here as reference temperature points, as shown in Fig. S1a. Steady-state temperature profiles are simulated here, since the crystallization process involves pulses with durations much longer than the thermal time constant (Fig. 2). Figure S1d shows the temperature data with different correction coefficients. The maximum temperature difference is 75 K when the boundary is straight, and it drops to 40 K when the correction coefficient equals 5. Figure S1e further shows the coefficient of temperature variance (defined as the standard deviation of temperatures across the points normalized by the average temperature), which confirms that $a = 5$ gives the optimal outcome.

Section II – Active metasurface design and measurement

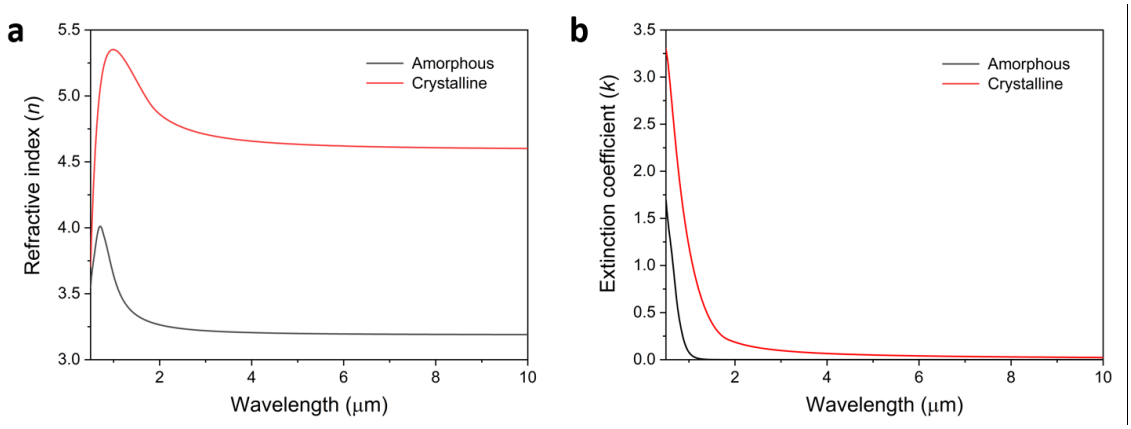

Fig. S2. Measured optical constants of GSST. The refractive indices n of GSST are 3.32 (amorphous) and 5.08 (crystalline) at 1550 nm wavelength, and the extinction coefficients are 0 (amorphous) and 0.35 (crystalline) at 1550 nm wavelength.

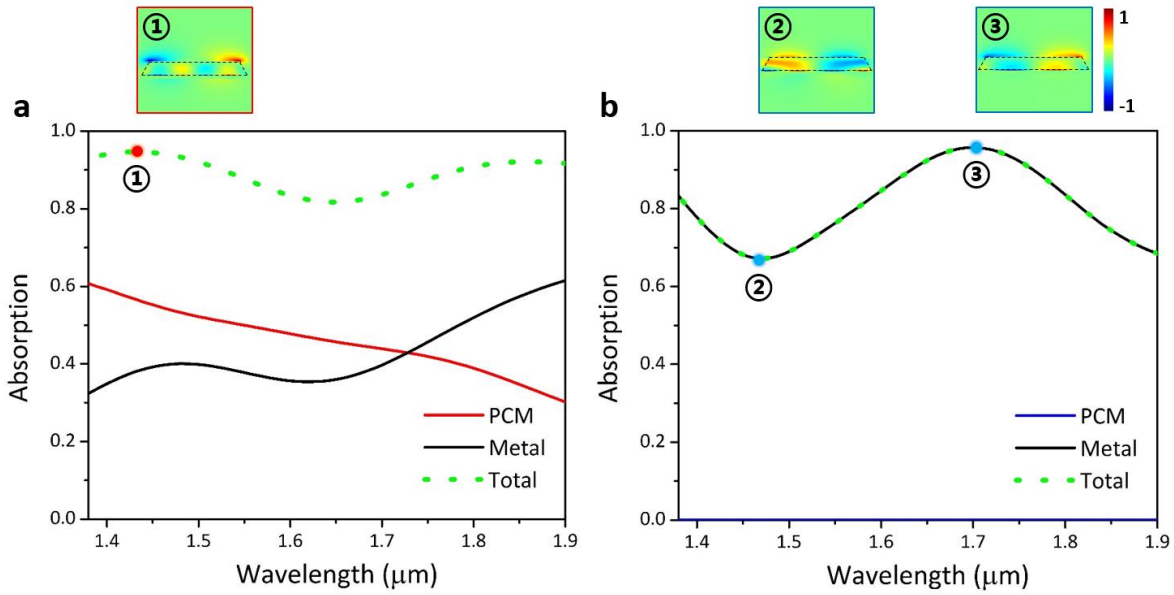

Fig. S3. Simulated spectra revealing absorption contributions from the metal heater and the PCM in the (a) crystalline and (b) amorphous states. Insets plot the electric field in the z-direction at selected wavelengths marked in the figures.

Fig. S2 shows the measured optical indices of the GSST phase change material obtained was measured using protocols described in our prior work[1]. The metasurface device presented in Fig. 3 in the main text consists of a periodic array of identical GSST meta-atoms. The geometry is chosen to achieve a large reflectance contrast in the near-IR wavelength. Insets of Fig. S3 show very different field distributions inside the meta-atoms in their amorphous versus crystalline states, indicate that the large refractive index modulation between the two states of GSST fundamentally alters the nature of the resonant mode supported in the meta-atoms. Therefore, our strategy to

obtain large optical contrast involves choosing geometric parameters of the meta-atoms and an operation wavelength such that it coincides with the reflectance minimum of one of the modes. To suppress reflection at the resonance minimum, the critical coupling condition must be met such that the coupling strength of the periodic array matches the optical dissipation rate of the mode[2]. To help understand the optical loss mechanisms in the device, Fig. S3 shows the simulated wavelength-dependent absorption by the PCM, the metal heater/reflector and the entire structure at crystalline and amorphous states. In the amorphous state, GSST features a remarkably low optical loss (e.g. extinction coefficient of amorphous GSST is $k = 1.8 \times 10^{-4}$ at 1550 nm wavelength according to waveguide cut-back measurements[3]), resulting in negligible absorption contributions across the spectral range. As a result, absorption is entirely attributed to the metal heater. The resonance can therefore be almost completely turned 'off' around 1.7 μm by matching the coupling strength (through tuning meta-atom geometries) to the absorption of metal to meet the critical coupling condition. Moving off the resonance gives rise to the reflectance maximum near 1.47 μm wavelength. In contrast, crystalline GSST does exhibits non-zero absorption in the near-IR (which gradually tapers off at longer wavelengths and almost vanishes in the mid-IR[1]). The peak shown in the crystalline state reflectance spectrum in Fig. 3b thus has a reduced amplitude due to the added loss contribution from PCM, which ultimately limits the switching contrast at the wavelength. Zoom-in plots of the modes marked as ①, ② and ③ can be found in Fig. S4. As can be inferred from the mode profiles, the modes are hybrid photonic-plasmonic modes. Similar hybrid photonic-plasmonic modes have been proposed and discussed in detail by Abdollahramezani *et al*[4]. As shown in Fig. S4, at amorphous state, the structure supports a magnetic-dipole-like mode ③. At crystalline state, on the other hand, due to the increased refractive index of PCM, as well as the close distance between the PCM meta-atom and the metals, the coupling between the dielectric mode and the surface plasmon polariton (SPP) mode generates a rather complex hybrid mode ①.

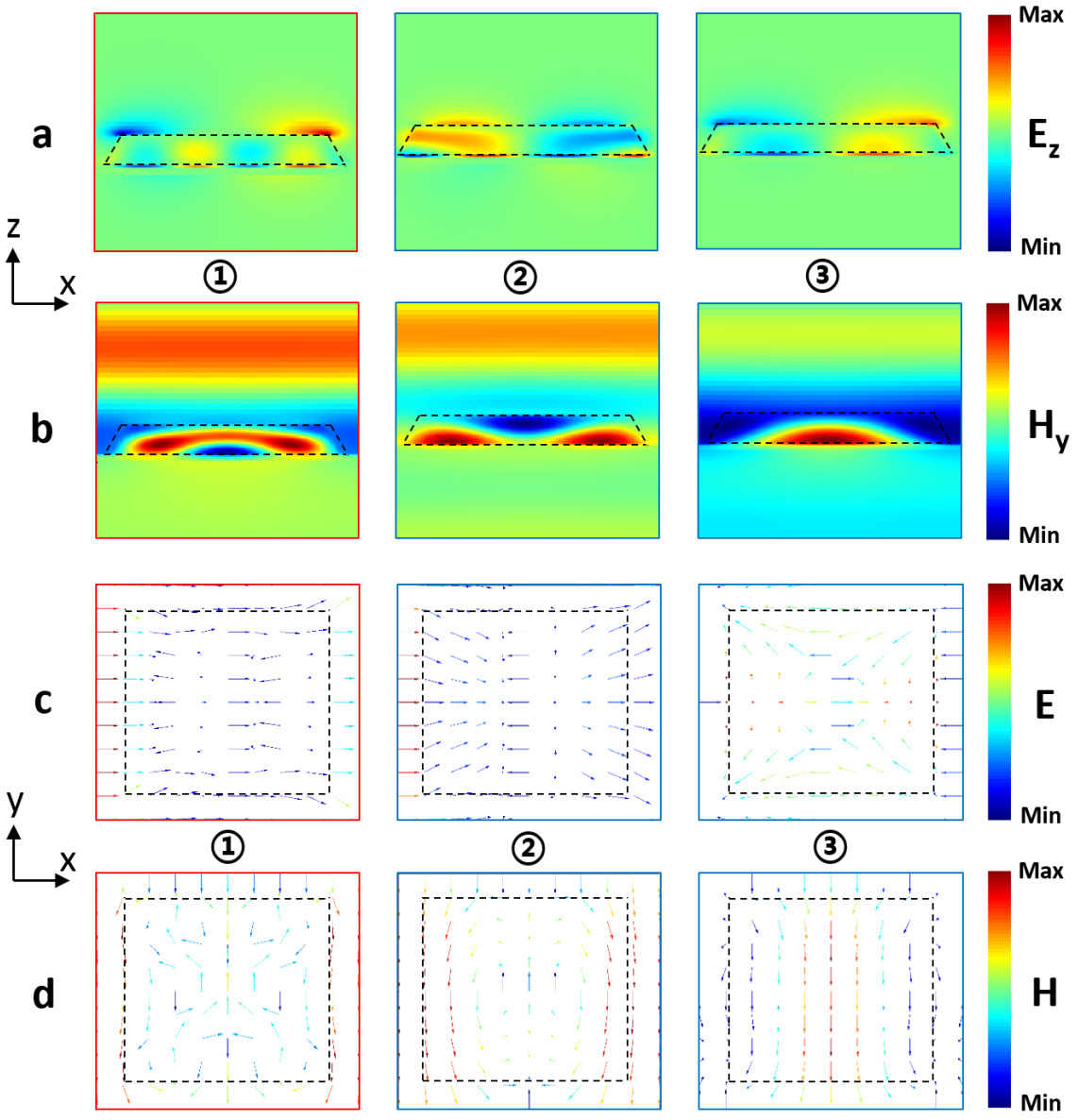

Fig. S4. (a, b) Simulated Ez (a) and Hy (b) profiles at selected wavelengths marked in Fig. S3. (c, d) Simulated amplitude profiles of electrical field (c) and magnetic field (d) at selected wavelengths marked in Fig. S3.

To verify that the optical contrast observed in our devices is attributed to the phase transition in PCM and complete reversible switching of PCM, we performed *in-situ* Raman measurements on the device presented in Fig. 3. Figure S5 shows the Raman spectra of the device under test at its as-deposited phase as well as its crystallized and re-amorphized states after 40 switching cycles. The excellent agreement between the Raman spectra corresponding to the as-deposited and re-amorphized states suggests that the material is fully (re-)amorphized, since the as-deposited state entirely comprises the amorphous phase as demonstrated in our prior work[1]. Therefore, our demonstrated electrical switching of PCM is complete and fully reversible.

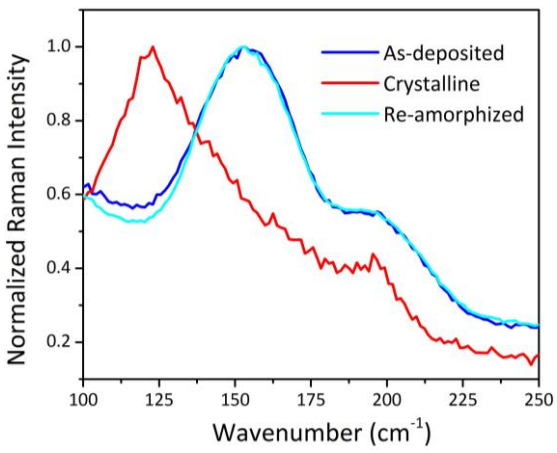

Fig. S5. Raman spectra of as-deposited, crystallized and re-amorphized GSST device.

Consistent with the Raman measurement results, our optical measurement data shown in Fig. 3c confirm that excellent switching reproducibility of the device up to 40 back-and-forth switching cycles. At further increased switching cycles, we started to observe progressive degradation of the metasurface, resulting in spectral shifts in the measured spectra. We note that this degradation is unlikely due to intrinsic material reliability issues, as we have previously demonstrated reproducible 1,000 cycle electrothermal switching of GSST without compromising the material quality[1]. The 1,000-cycle switching experiment was performed on metal heaters with similar layer structures albeit with much smaller size (10 μm × 10 μm square), which implies considerably reduced temperature non-uniformity across the heaters. The observed degradation is therefore probably attributed to local temperature surges at heater hot spots which ultimately results in failure. The heater temperature uniformity and hence device reliability can be further enhanced by optimizing heater designs with more geometric degrees of freedom, a new direction which we will discuss in another forthcoming publication.

Section III – Evaluation of GSST meta-atom crystallization kinetics

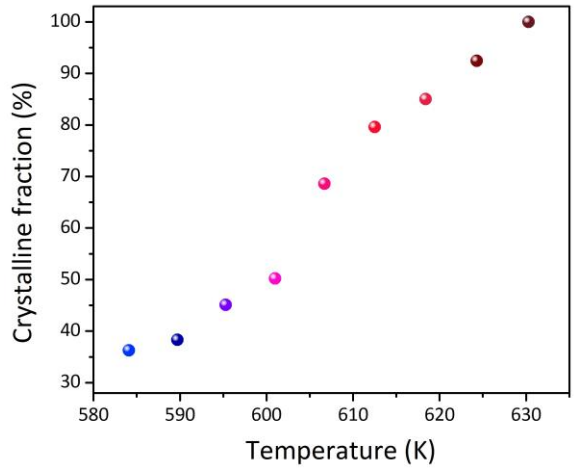

Fig. S6. Volume fraction of crystalline phase associated with the different intermediate states as a function of the corresponding crystallization temperatures.

Figure S6 gives a quantitative description of the GSST meta-atom crystallization kinetics by presenting the volume fractions of crystalline phase in different intermediate states as a function of the crystallization temperature (taken as the temperature in the middle plane inside the PCM layer and at the center of the heater) at which the corresponding intermediate state is obtained. The same data were plotted in Fig. 4c in the main text showing the crystallization pulse voltage dependence. To obtain the crystalline fractions associated with different intermediate states, we first use data in Fig. 4a and FDTD simulations to extract the refractive index of PCM at each intermediate state. We then apply an effective medium theory based on the Lorentz–Lorenz equation to compute the crystalline phase volume fraction for each refractive index value[5]. Specifically, the effective permittivity of GSST ϵ_{eff} at any crystalline phase volume fraction m, ranging from 0 to 1, is calculated via:

$$\frac{\epsilon_{\text{eff}}(\lambda)-1}{\epsilon_{\text{eff}}(\lambda)+2} = m \times \frac{\epsilon_{\text{c}}(\lambda)-1}{\epsilon_{\text{c}}(\lambda)+2} + (1-m) \times \frac{\epsilon_{\text{a}}(\lambda)-1}{\epsilon_{\text{a}}(\lambda)+2}$$

where λ is the wavelength in free space, and $\epsilon_{\text{c}}(\lambda)$ and $\epsilon_{\text{a}}(\lambda)$ are the permittivities of GSST in crystalline and amorphous states, respectively. Here the complex refractive index $n(\lambda)+ik(\lambda)$ of the material was inferred from fitting the experimental spectra with FDTD simulations and is related to the effective permittivity $\epsilon_{\text{eff}}(\lambda)$ by $\sqrt{\epsilon_{\text{eff}}(\lambda)} = n(\lambda)+ik(\lambda)$. Similar effective medium treatment has been applied to phase transition oxide materials as well[6].

The PCM temperature during crystallization was separately computed using FEM simulations based on the experimental electrical pulse parameters and following modeling protocols described in Methods. Since the crystallization pulse duration is much larger than the thermal time constant of the heater, we model the crystallization process as a steady-state heating problem. The phase composition and temperature data were then combined to produce Fig. S6.

Although the change of the crystalline fraction as a function of temperature is not solely determined by the crystallization rate, there is an optimal temperature range (in our case around 600 – 615 K) that the crystallization fraction increases in a fastest manner. This can be explained by examining the phase transformation mechanism of amorphous solids[7], which involves both nucleation and growth. For nucleation, both the term of activation energy barrier and the term of activation energy for atomic migration are temperature dependent. When temperature is lower, the first term increases while the second term decreases. This results in a maximum nucleation rate above T_g (glass transition temperature). Growth exhibits a similar behavior[8], and its maximum rate typically occurs at a higher temperature somewhere between T_g and T_m (melting point). This normally results in a maximum in the overall crystallization rate, which was confirmed for example by experiments characterizing crystallization kinetics of $Ge_2Sb_2Te_5$[9]. Therefore, the maximum

crystalline fraction increasing rate within the 600 – 615 K temperature range is expected as a consequence of the crystallization rate temperature dependence. The crystallization kinetics should be properly taken into consideration and calibrated before implementing multi-state switching with functional PCM devices.

Section IV – Huygens' surface beam deflector design

Figure S7 depicts the design of the reconfigurable beam deflector. The polarization-insensitive reconfigurable deflector is designed to operate as a Huygens' surface[10] that couples to the +1 mode in the amorphous state and to the 0th order mode in the crystalline state. The deflection angle of the +1 mode is calculated from the grating equation by setting the grating period equal to the supercell period in the deflection plane (A_x). Once the deflection angle has been selected, the phase gradient that the meta-atoms must satisfy in the amorphous state is determined from the Generalized Snell's Law[11], while the phase gradient in the crystalline state must be zero to yield an undeflected beam. The unit cell size of the meta-atoms is kept below one wavelength in the direction perpendicular to the deflection plane (A_y) to suppress spurious out of plane diffraction modes. This approach could also be used for switching between the +1 and -1 modes by setting the phase gradient of the crystalline state to be opposite of that in the amorphous state.

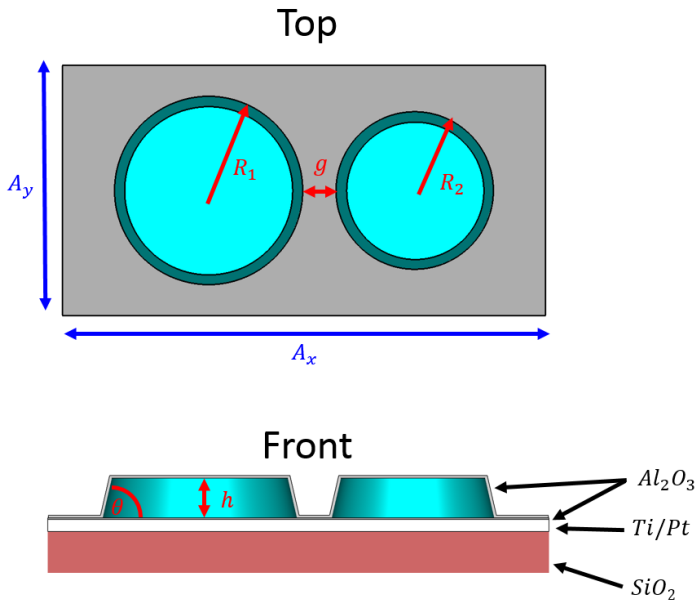

R_1	0.56 μm
R_2	0.47 μm
g	0.2 μm
A_x	2.9 μm
A_y	1.5 μm
θ	77°
h	0.23 μm

Fig. S7. Schematic of reconfigurable GSST beam deflector. Each structure has unit cell size, $A_x/2$ by A_y, with the structures off-centered so that the separation is shorter on one side. Radii and gap lengths are measured at the bottom of the tapered cylinders. The Pt/Ti alloy heating elements is 70 nm thick. The Al_2O_3 layer between the heater and the meta-atoms is 10 nm thick and the Al_2O_3 capping layer is 15 nm thick. Listed dimensions for the GSST structures (R_1, R_2, and h) are for the amorphous state and shrink to 96% in the crystalline state.

Under certain conditions, Huygens' surfaces can be aggressively discretized to reduce the number of required structures to meet design goals[12]. This creates significant advantages to ease the design of the proposed beam deflector: 1) Since the meta-atoms for the design must simultaneously satisfy four conditions while possessing high reflectance (proper phase for both TE and TM polarizations in both amorphous and crystalline states), it becomes increasingly difficult to satisfy these conditions as the number of structures increases. 2) Typically, with Huygens' surfaces, the meta-atom set must achieve full 2π phase coverage to be effective. This can necessitate using structures that are difficult to fabricate, have low reflectance, or don't possess 4-fold rotational symmetry for polarization insensitivity. By using the method outlined in the

following paragraph, beam-deflection can be achieved with only two structures per supercell and with total phase coverage less than π, thus enabling the use of simple, robust, cylindrical structures.

In a typical Huygens' surface design, where the meta-atoms are evenly spaced, a design with only two meta-atoms would not work, because the two meta-atoms would necessarily be 180 degrees out of phase to satisfy the Generalized Snell's Law, and thus would not yield a preferred deflection direction between the +1 and -1 diffraction modes. Alternatively, the spacing of the meta-atoms can be reduced if accompanied by a corresponding reduction in the phase difference between meta-atoms, such that the phase gradient and supercell period, A_x, are preserved. Since the total phase difference across the supercell must be 2π, the phase difference, $\Delta\phi$, between two structures separated by a distance, d, must obey:

$$\frac{\Delta\varphi}{2\pi} = \frac{d}{A} \quad \rightarrow \quad \Delta\varphi = \frac{2\pi d}{A}$$

This approach is similar to using coupled dielectric structures to achieve beam deflection[13]. Since the coupling effect between dielectric structures is typically weak, these two approaches may be identical, but with the Huygens' surface model having a more intuitive design process and possibly being a more accurate physical description.

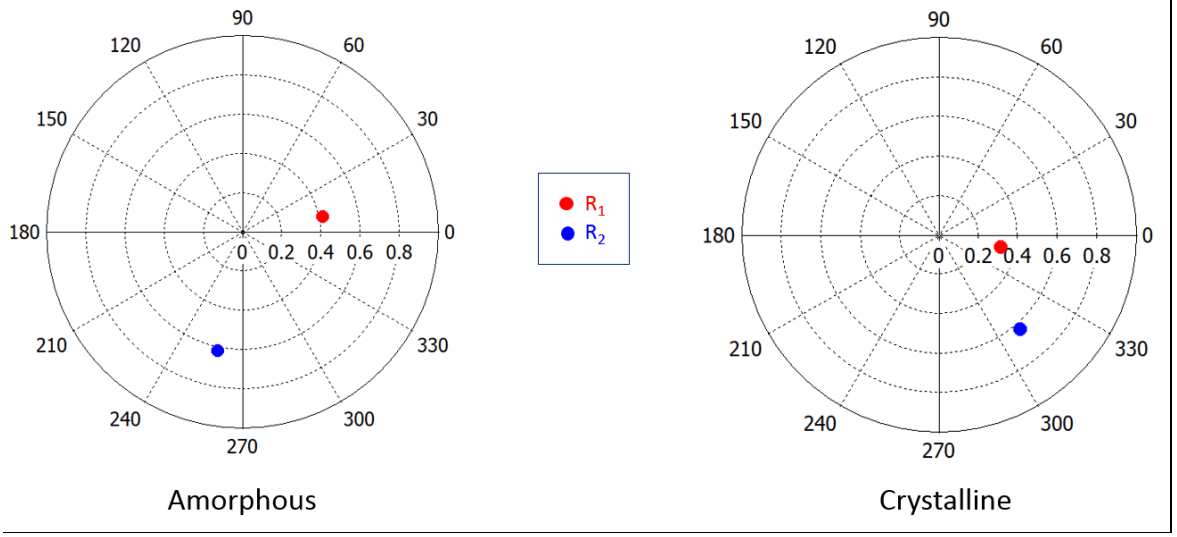

Fig. S8. Polar plots of reflection coefficients for the individual meta-atoms used in the design at their amorphous (left) state and crystalline state (right). R_1 is 0.56 μm and R_2 is 0.47 μm.

In our modeling, S-parameter and far field radiation pattern calculations are made with CST Microwave Studio commercial full-wave software using the frequency solver under unit cell boundary conditions. Material parameters for the metallic heating element and both the amorphous and crystalline states of GSST are obtained from empirical data. Fig. S8 shows the phase and amplitude response of the individual meta-atoms that are used in the deflector design. The simulated deflection efficiencies in both states are summarized in Table S1. The predicted crosstalk is 11.4 dB according to the simulation results.

Table S1. Simulated deflection efficiency of the meta-deflector.

	+1 order	0 order	-1 order
Amorphous	10.7%	6.9%	4.1%
Crystalline	2.8%	24.8%	1.9%

Section V – Future outlook

Further increasing the meta-atom thickness will give more room for phase control and possibly better device performance. There is no fundamental limit on the GSST film thickness that we can deposit. We have used a much thicker GSST film of 1.1 μm to demonstrate a varifocal metalens[14]. However, the critical cooling rate (R_c) needed for re-amorphization imposes a limit on thickness of films that can be reversibly switched. R_c defines the minimum cooling rate necessary to kinetically bypass crystallization when a liquid is quenched to form the amorphous state. In a PCM film, the actual cooling rate is determined by the film thickness as well as the thermal conductivity of the film. R_c therefore dictates the maximum PCM film thickness t_{max} where complete re-amorphization (aka complete suppression of crystallization throughout the entire volume) is possible[15]:

$$t_{max} \approx \sqrt{\frac{\alpha \cdot (T_{liq} - T_{nose})}{R_c}}$$

where T_{liq} and T_{nose} denote the liquidus temperature and the 'nose' temperature in the temperature-time-transformation (TTT) plot, respectively. The equation suggests an important trade-off in PCM design: increasing crystallization rate (i.e. switching speed) comes with the expense of reduced reversibly switchable film thickness. For the classical GST-225 alloy, its fast crystallization rate points to a maximum switchable film thickness of approximately 70 nm, which is in agreement with experimental reports of GST-based devices[16,17]. That is another reason (in addition to its low loss) we opt for GSST which offers slower crystallization kinetics for the metasurface design. Since we have not quantitatively characterized the crystallization kinetics of GSST, it is not possible to provide an accurate estimate of the switchable GSST thickness. If assuming a crystallization time in the μs to sub-ms scale, the switchable GSST thickness should exceed 1 μm. This is certainly an important direction we are pursuing right now. Further work is ongoing to increase the meta-atom thickness used in the devices.

Operation speed is another important criteria for reconfigurable photonic devices. The amorphization pulse duration is 5 μs, and the amorphization time is limited by the thermal time constant of the system. We choose a relatively long crystallization pulse duration of 500 ms, which is optimized for the voltage we used to ensure minimal temperature nonuniformity across the large aperture (as shown in Fig. 2b) as well as complete crystallization to render maximum index contrast. For smaller pixels (10 μm × 10 μm) we were able to perform switching with 1 μs amorphization pulse and 1 ms crystallization pulse given the smaller thermal time constant and the negligible temperature nonuniformity. Therefore, further enhancing the switching speed will require optimization of the heater design, for instance by introducing more geometric variables in addition to boundary curvature. Ultimately, the crystallization pulse duration is limited by the intrinsic crystallization kinetics of GSST meta-atoms, which is likely in the sub-ms regime.

We observed that while the device can still operate beyond 50 switching cycles, the reflectance spectra of the crystalline state start to exhibit drifts greater than the 3.5% bar illustrated in Fig. 3c, which is why we did not claim a switching lifetime beyond 50 cycles in the first place. Close inspection of the devices reveals that scattered defects appeared at the edges of the device, which accounts for the deviation from the pristine spectrum. Preliminary Raman studies suggest that the defects correspond to amorphized region which fail to crystallize upon subsequent heating cycles. Since we have previously demonstrated 1,000 cycle of highly reproducible switching of GSST using the electrothermal method[1], the defects are not a signature of limited material cyclability. The consistent appearance of the defects at device edges seems to indicate that this has to do with

residual thermal nonuniformity of the device. One possible explanation is that the defective spots fail to crystalize because of elemental migration caused by thermal cycling, which is a common failure mechanism in phase change memories[18]. Melting and subsequent liquid phase mass transport during the amorphization cycle have previously been found to 'heal' such defects and extend lifetime of memory cells[19]. However, such homogenization is incomplete at the edges where the temperature is lower, and hence the dwell time at liquid state as well as the thermally activated atomic transport are reduced. As a consequence, defects preferentially form at the device edges. Therefore, further enhancing the long-term stability will require optimization of the temperature uniformity, which can be achieved by further improving the heater design, for instance by introducing more geometric variables in addition to boundary curvature. Further work is still ongoing to elucidate the nature and origin of such defects.

References

1. Zhang, Y. *et al.* Broadband transparent optical phase change materials for high-performance nonvolatile photonics. *Nat. Commun.* **10**, 4279 (2019).
2. Zanotto, S. Weak coupling, strong coupling, critical coupling and fano resonances: A unifying vision. in *Springer Series in Optical Sciences* vol. 219 551–570 (Springer Verlag, 2018).
3. Zhang, Q. *et al.* Broadband nonvolatile photonic switching based on optical phase change materials: beyond the classical figure-of-merit. *Opt. Lett.* **43**, 94 (2018).
4. Abdollahramezani, S. *et al.* Dynamic hybrid metasurfaces. *arXiv:2008.03905* (2020).
5. Voshchinnikov, N. V., Videen, G. & Henning, T. Effective medium theories for irregular fluffy structures: Aggregation of small particles. *Appl. Opt.* **46**, 4065–4072 (2007).
6. Frame, J. D., Green, N. G. & Fang, X. Modified Maxwell Garnett model for hysteresis in phase change materials. *Opt. Mater. Express* **8**, 1988 (2018).
7. Porter, D. & Easterling, K. *Phase transformations in metals and alloys*. (CRC Press, 2009).
8. Descamps, M. & Dudognon, E. Crystallization from the amorphous state: Nucleation-growth decoupling, polymorphism interplay, and the role of interfaces. *Journal of Pharmaceutical Sciences* vol. 103 2615–2628 (2014).
9. Orava, J., Greer, A. L., Gholipour, B., Hewak, D. W. & Smith, C. E. Characterization of supercooled liquid Ge2Sb2Te5 and its crystallization by ultrafast-heating calorimetry. *Nat. Mater.* **11**, 279–283 (2012).
10. Decker, M. *et al.* High-Efficiency Dielectric Huygens' Surfaces. *Adv. Opt. Mater.* **3**, 813–820 (2015).
11. Yu, N. *et al.* Light Propagation with Phase Discontinuities Reflection and Refraction. *Science.* **334**, 333–337 (2011).
12. Chen, M., Kim, M., Wong, A. M. H. & Eleftheriades, G. V. Huygens' metasurfaces from microwaves to optics: A review. *Nanophotonics* **7**, 1207–1231 (2018).
13. Paniagua-Dom ńguez, R. *et al.* A Metalens with a Near-Unity Numerical Aperture. *Nano Lett.* **18**, 2124–2132 (2018).
14. Shalaginov, M. Y. *et al.* Reconfigurable all-dielectric metalens with diffraction limited performance. *arXiv:1911.12970* (2019).
15. Musgraves, J. D., Hu, J. & Calvez, L. *Springer Handbook of Glass*. (Springer International Publishing, 2019). doi:10.1007/978-3-319-93728-1.
16. Wang, Q. *et al.* Optically reconfigurable metasurfaces and photonic devices based on phase change materials. *Nat. Photonics* **10**, 60–65 (2016).
17. Ruiz De Galarreta, C. *et al.* Reconfigurable multilevel control of hybrid all-dielectric phase-change metasurfaces. *Optica* **7**, 476–484 (2020).
18. Oh, S. H. *et al.* In situ TEM observation of void formation and migration in phase change memory devices with confined nanoscale Ge2Sb2Te5. *Nanoscale Adv.* **2**, 3841–3848 (2020).
19. Du, P. Y. *et al.* The impact of melting during reset operation on the reliability of phase change memory. in *IEEE International Reliability Physics Symposium Proceedings* (2012). doi:10.1109/IRPS.2012.6241872.